



## Large-scale coherent structures in the atmosphere over a flat terrain

Alcayaga, Leonardo; Larsen, Gunner Chr.; Kelly, Mark ; Mann, Jakob

*Published in:*  
Journal of Physics: Conference Series

*Link to article, DOI:*  
[10.1088/1742-6596/1618/6/062030](https://doi.org/10.1088/1742-6596/1618/6/062030)

*Publication date:*  
2020

*Document Version*  
Publisher's PDF, also known as Version of record

[Link back to DTU Orbit](#)

*Citation (APA):*  
Alcayaga, L., Larsen, G. C., Kelly, M., & Mann, J. (2020). Large-scale coherent structures in the atmosphere over a flat terrain. *Journal of Physics: Conference Series*, 1618(6), Article 062030. <https://doi.org/10.1088/1742-6596/1618/6/062030>

---

### General rights

Copyright and moral rights for the publications made accessible in the public portal are retained by the authors and/or other copyright owners and it is a condition of accessing publications that users recognise and abide by the legal requirements associated with these rights.

- Users may download and print one copy of any publication from the public portal for the purpose of private study or research.
- You may not further distribute the material or use it for any profit-making activity or commercial gain
- You may freely distribute the URL identifying the publication in the public portal

If you believe that this document breaches copyright please contact us providing details, and we will remove access to the work immediately and investigate your claim.

PAPER • OPEN ACCESS

## Large-scale coherent structures in the atmosphere over a flat terrain

To cite this article: Leonardo Alcayaga *et al* 2020 *J. Phys.: Conf. Ser.* **1618** 062030

View the [article online](#) for updates and enhancements.



**IOP | ebooks™**

Bringing together innovative digital publishing with leading authors from the global scientific community.

Start exploring the collection—download the first chapter of every title for free.

# Large-scale coherent structures in the atmosphere over a flat terrain

Leonardo Alcayaga, Gunner Chr. Larsen, Mark Kelly, Jakob Mann

DTU Wind Energy, Frederiksborgvej 399, 4000 Roskilde, Denmark

E-mail: lalc@dtu.dk

**Abstract.** Large-scale coherent motions in the atmospheric boundary layer are investigated from field measurements made with two scanning wind lidars over a two-dimensional domain covering approximately  $50 \text{ km}^2$ . The size, isotropy and two-point statistics of the coherent structures, show their influence on wind field homogeneity and local conditions that wind turbines might experience within a wind farm. For neutral atmospheric stability and high wind conditions, most of these structures are observed to be narrow streaks of low streamwise momentum having positive vertical velocity component (ejections), extending several kilometers. The results shown here are consistent with numerical simulations of atmospheric flows under similar conditions, and scale experiments made in laboratories.

## 1. Introduction

Organized or coherent motions have been widely observed within many turbulent flows: in laboratory settings [1, 2], in atmospheric boundary layer flow observations [3, 4] and in atmospheric flow simulations [5]. Methods to identify and analyze them have consequently developed in recent decades [6, 7]. Large coherent motions with spatial sizes ranging up to the characteristic length scale of a wind farm are of particular interest from a wind energy perspective, since the characterization of such structures and their large-scale velocity fluctuations, is important to explain and model power production, loading and wake dynamics (see [8]). The development of wind lidars has opened the possibility to observe large wind fields across many scales, both in space and time, which poses a unique opportunity to study organized motions over different types of terrain. Based on data from dual WindScanner long-range lidars [9], and the subsequent reconstruction of horizontal velocity fields covering an area of roughly  $50 \text{ km}^2$ , this work has several aims: identifying and characterizing large atmospheric coherent structures at different heights, under neutral stability conditions; and finding homogeneity and turbulence characteristics of the flow field, including dominant length scales and degree of anisotropy. Previous studies [4] used observations from lidars to characterize such structures in the atmospheric surface layer over flat terrain, covering areas of similar extent at approximately 50 m above ground level, and were able to identify near-surface streaks and open (convective) cells during calm wind conditions. The data presented here also show similar large scale motions at these heights, but extend these observations to 200 m above the ground level, a height that is well above the surface layer and the effect of the site elevation and tree cover. Flow under neutral stability conditions is analyzed in terms of homogeneity and two-point correlation statistics.



## 2. Østerild ‘Balconies’ Experiment

The results presented here are based on lidar measurements [10], obtained at the Østerild Test Centre located in northern Jutland, Denmark, see Figure 1. The aim of this experiment was to characterize the horizontal flow field above a flat, heterogeneous forested landscape at two heights relevant for wind energy applications. Known as the Østerild Balconies Experiment [11, 12], the horizontal velocity data covers a large area (around 50 km<sup>2</sup>), with the possibility of characterizing flow patterns in a wide range of scales, both in time and space.

The Balconies Experiment consisted of two measuring phases (see Table 1) with two long-range WindScanners performing Plan Position Indicator (PPI) scanning patterns, aligned along a North-South axis and installed at 50 m a.g.l. during phase 1 and 200 m a.g.l. in phase 2. WindScanners [9] consist of two or more spatially separated lidars, which are synchronized to perform coherent scanning patterns, allowing the retrieval of two- or three-dimensional velocity vectors at different points in space. These experiments were conducted between April and August of 2016. In each phase, the northern and southern lidars scanned in respectively the westerly and easterly direction relative to the corresponding meteorological masts, where they were installed. The data used in this study originated from both phases of the experiment, however, with PPIs pointing to the west only. The reasons for this is that scans pointing to the east have enough data for analysis only for phase 1. For more details about the experiment, lidars and terrain characteristics see [12].

**Table 1.** Balconies experiment. The scans are neither instantaneous nor totally synchronous, with a horizontal sweep speed of 2°/s in the azimuthal direction over a range of 90° and total time of 45 s per scan. The range gate length for both WindScanners is 35 m.

Phase	Measurement start	Measurement end
50 m a.g.l. (1)	2016-04-12 12:45:41	2016-06-17 12:48:01
200 m a.g.l. (2)	2016-06-29 13:35:56	2016-08-12 09:09:55
Scanner	Location coordinates, [m]	Scanning pattern, west
Southern lidar	492768.8 (East) 6322832.3 (North)	344°-256°, 2° azimuthal steps
Northern lidar	492768.7 (East) 6327082.4 (North)	196°-284°, 2° azimuthal steps

## 3. Characterization of large-scale motions

### 3.1. Velocity field reconstruction from lidars

In order to reconstruct the two-dimensional velocity field, the dual Windscanner data was used under the assumption that both the north and south scans were quasi-simultaneous over a period of 45 s, equivalent to the time spent for each scan to be completed. The filtered line-of-sight wind speeds ( $V_{LOS}$ ) obtained from each lidar represent a projection of the horizontal velocity components onto the lidar beam with azimuthal position  $\theta$  as

$$V_{LOS} = V_x \cos \theta + V_y \sin \theta, \quad (1)$$

and as a function of the azimuthal position of the two lidar beams at a specific point in space:  $\theta_1(\mathbf{x})$  and  $\theta_2(\mathbf{x})$ . The horizontal velocity components,  $V_x(\mathbf{x})$  and  $V_y(\mathbf{x})$ , can be retrieved using

$$V_x(\mathbf{x}) = \frac{-V_{LOS,1}(\mathbf{x}) \sin(\theta_2(\mathbf{x})) + V_{LOS,2}(\mathbf{x}) \sin(\theta_1(\mathbf{x}))}{\sin(\theta_1(\mathbf{x}) - \theta_2(\mathbf{x}))} \quad (2)$$

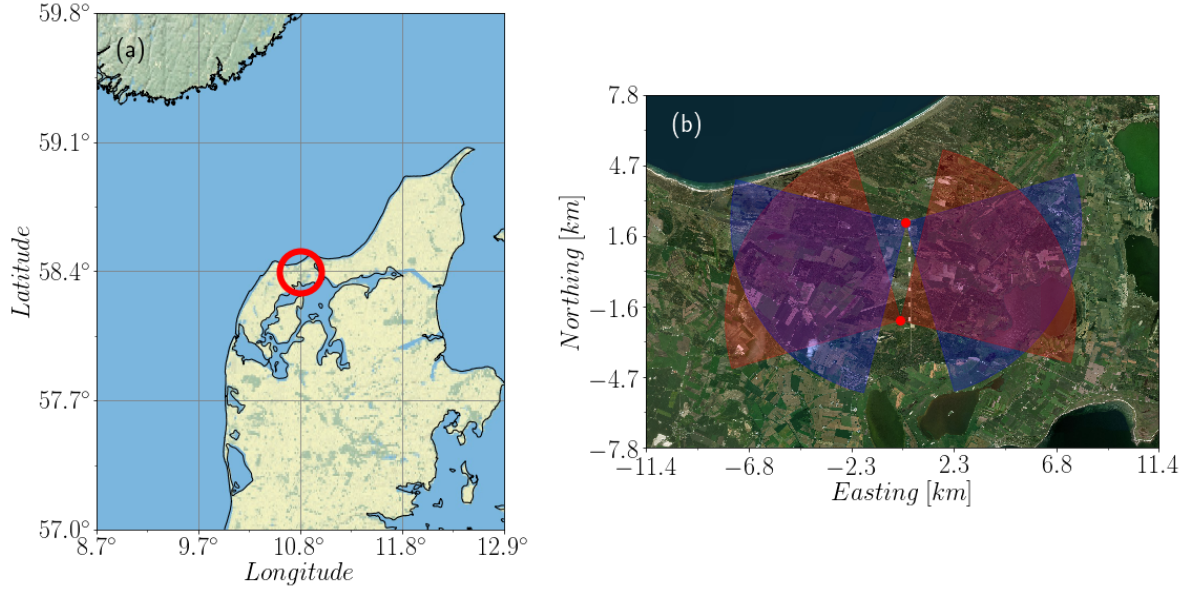


**Figure 1.** (a) Location of the Østerild Turbine Test Center, where the Balconies Experiment was performed, northern Jutland, Denmark (copyright 2009 Esri). (b) Detail of the test center site, with the location of the meteorological masts where north (blue) and south (red) WindScanners were installed. During the measurement campaign the PPI scans pointed both west in some periods and east in other periods (copyright 2017 DigitalGlobe, Inc.).

and

$$V_y(\mathbf{x}) = \frac{V_{LOS,1}(\mathbf{x}) \cos(\theta_2(\mathbf{x})) - V_{LOS,2} \cos(\theta_1(\mathbf{x}))}{\sin(\theta_1(\mathbf{x}) - \theta_2(\mathbf{x}))}. \quad (3)$$

The  $V_{LOS}$  values of each scan, that is resolved in a polar grid coordinate system, are cubic spline interpolated onto a Cartesian grid using a Delaunay triangulation, rejecting values of invalid observations detected during data filtering (for details of the filtering technique see [13]). The resulting scans are then used to reconstruct two-dimensional wind fields. A final transformation is made on the instantaneous two-dimensional wind fields to obtain streamwise and lateral velocity components ( $u_1$  and  $u_2$ ), using a 10-minute temporally and spatially averaged velocity vector to obtain the mean wind direction.

### 3.2. Two-point correlation and integral length scales

For displacements  $\tau$  in the streamwise and  $\eta$  in the cross-wind directions, the two-point correlations of velocity components ( $R_{ij}$ ) and corresponding correlation function ( $\rho_{ij}$ ) are defined by

$$R_{ij}(\tau, \eta) = \frac{1}{N} \sum u_i(x_1, x_2) u_j(x_1 + \tau, x_2 + \eta); \quad \rho_{ij}(\tau, \eta) = \frac{R_{ij}(\tau, \eta)}{\sqrt{R_{ii}(0, 0) R_{jj}(0, 0)}}. \quad (4)$$

Even though correlations are two-dimensional fields, the integral length scales  $L_{u_i, x_i}$ , which correspond to length scales of fluctuations of the  $u_i$  velocity components in the  $x_i$  directions, are estimated by integrating  $\rho_{ii}(\tau, \eta)$  along each displacement axis [14]:

$$L_{u_i, x_1} = \int_0^{x_0} \rho_{ii}(x_1, 0) dx_1; \quad L_{u_i, x_2} = \int_0^{x_0} \rho_{ii}(0, x_2) dx_2, \quad (5)$$

where  $x_0$  is the first zero crossing.

For increasing offsets  $(\tau, \eta)$ , the decreasing number of points in the overlapping area,  $N$  in (4), will bias the estimate of the corresponding correlation,  $R_{ii}^N(\tau, \eta)$ . Assuming exponential decay in  $\rho_{ij}(\tau, \eta)$ , this bias increases approximately with  $N$  according to (see [15])

$$\langle R_{ii}^N(\tau, \eta) \rangle - R_{ii}(\tau, \eta) \approx 2R_{ii}(0, 0) \frac{L_{u_i, x_1} L_{u_i, x_2}}{N dx dy}, \quad (6)$$

where  $dx$  and  $dy$  are the grid element sizes from wind field reconstruction and  $\langle . \rangle$  denotes ensemble average. The minimum value of  $N$  then will come from displacements  $(\tau, \eta)$  with values of  $\sqrt{2 \frac{L_{u_i, x_1} L_{u_i, x_2}}{N dx dy}}$  no larger than 15%. This limit is usually not reached before zero crossings in  $(\tau, \eta)$ , and  $L_{u_i, x_i}$  can be estimated properly. When this is not the case, the total number of points in the individual wind field is used.

### 3.3. Stability classification

To determine the stability conditions, data from three-dimensional sonic anemometers at the two meteorological masts where WindScanners were installed were used to determine the momentum and heat fluxes at several heights. From these data, the Obukhov length is defined as

$$L = - \frac{u_*^3 T}{kgw\theta}, \quad (7)$$

where  $u_* = (\overline{uw^2} + \overline{vw^2})^{1/4}$  is the friction velocity that is determined by stream, spanwise and vertical velocity fluctuations ( $\{u, v, w\} = \{u_1, u_2, u_3\}$ ), respectively, and  $\overline{w\theta}$  represents the vertical heat flux in the form of the covariance between  $w$  and fluctuations in the potential temperature  $\theta$ . Along with the von Kármán constant  $k$  and gravitational acceleration  $g$ , the relation between buoyancy and mechanical turbulence generation mechanisms is represented in this length scale and is used here as a measure of the stability of the flow. Neutral conditions are defined as flows with  $|L|^{-1} < 0.002 \text{ m}^{-1}$ , unstable conditions by  $L^{-1} < -0.002 \text{ m}^{-1}$ , and stable conditions by  $L^{-1} > 0.002 \text{ m}^{-1}$ .

## 4. Results

### 4.1. Stability conditions

From 10-minute averages the inverse Obukhov lengths  $L^{-1}$  observed for phases 1 ( $z = 50 \text{ m}$ ) and 2 ( $z = 200 \text{ m}$ ) are shown in Figure 2 following [16]. Unstable, stable, and neutral conditions are seen to be more or less equally distributed for the measured periods. The analysis here is focused on wind fields under neutral or near-neutral conditions, which for both phases of the Balconies Experiment corresponds to 26-27% of the total number of lidar scans. Unstable and stable conditions account for 39% and 35% of the cases in phase 1, respectively, and 39% and 35% in phase 2.

### 4.2. Horizontal wind field under near-neutral conditions

Wind fields reconstructed under neutral conditions show different characteristics depending on height. Figure 3 shows a 30-min average of the streamwise velocity component ( $U$ ) during strong westerly winds observed during phases 1 and 2, with scans pointing toward the West. The influence of the terrain on the wind field at 50 m above ground level is clear. Large patches of forest correspond to lower wind speeds at the center, and in a large north-east portion of the scanning area. This 30-min feature of the lower- $z$  scans is in line with the results found for the average wind speed over the entire campaign shown by [12]. A group of wind turbines, shown as an empty stripe in Figure 3(a), also influence the mean wind speeds. At a first sight, terrain effects and obstacles play an important role in the inhomogeneity of the horizontal wind field.

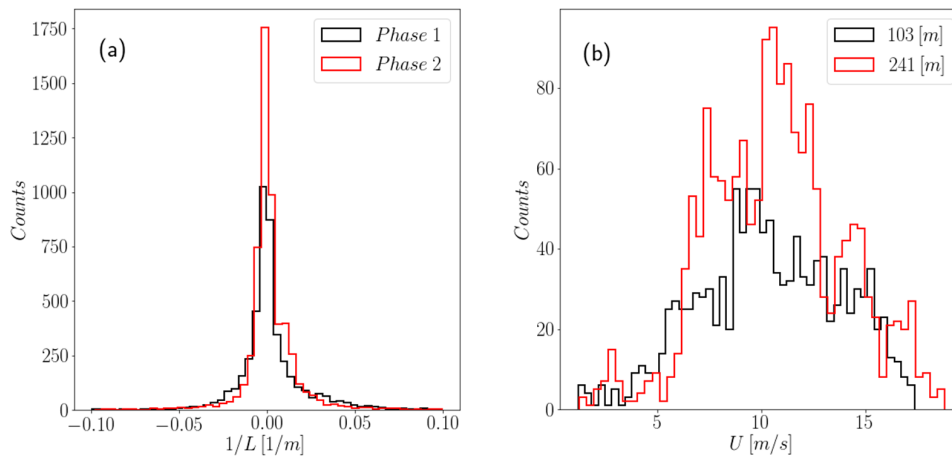


**Figure 2.** (a) Distribution of  $1/L$  for phase 1 and phase 2 of the Balconies experiment. Neutral conditions lay within the range of  $-0.002$  and  $0.002$  of  $1/L$ , and corresponds to approximately 26% of the total number of lidar scans for both phases of the experiment. (b) 10-min streamwise mean wind speed during neutral conditions at two heights close to the lidar's elevation.

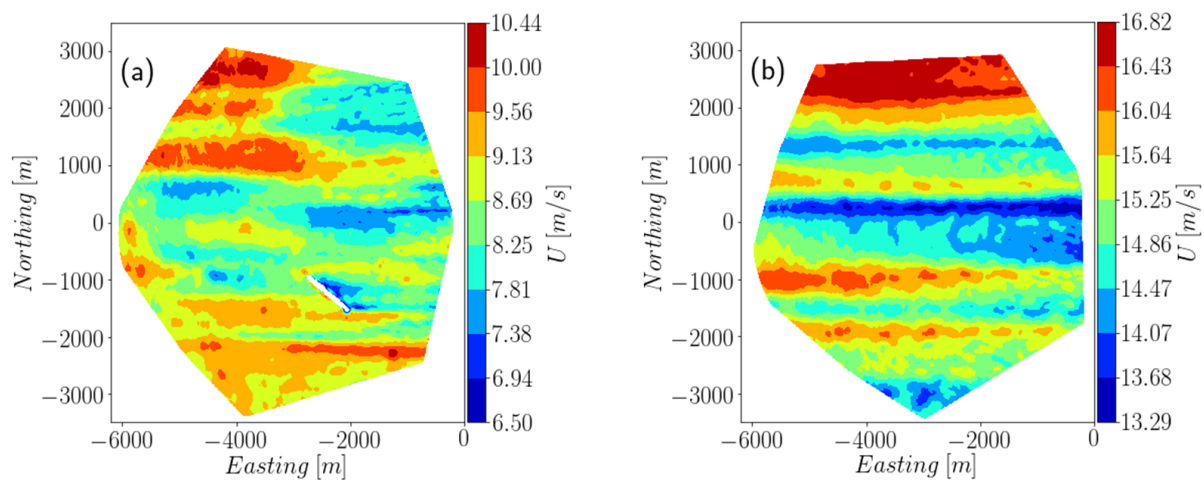


**Figure 3.** Streamwise wind component field during both phases of Balconies experiment. The fields shown correspond to a particular 30-minute average of a series of scans taken during neutral conditions and strong westerly winds. Fields are aligned with the mean wind direction. (a) Phase 1 at 50 m above ground level. The effect of the terrain is clear at low speed regions over patches of forested terrain and a group of turbines and their wakes in the voided south-east stripe. (b) Phase 2, at 200 m above ground level. The inhomogeneity of the wind field comes from persistent steaks of low and high wind speed, and an area of high wind speed in the north of the scan corresponding to the upwind influence of flow over water.

Persistent organized flow structures, as it will be seen later, are smeared by their own meandering movement when the averaging window is larger than the advective time scale characteristic of the domain size,  $T_{advec} = U/L_{domain}$ .

The situation is different when we look above the surface layer<sup>1</sup>, as shown in Fig. 3(b). At 200 m, the effect of forest patches or obstacles on the wind field is not clear. More organized persistent structures in the form of large streaks can be seen, with locations from north to south with little variation even for long time windows. The only exception is a wide high wind speed strip in the northern part of the scan, which can be attributed to the sea surface influence. Not surprisingly, the persistence of these structures extent up to an area in the eastern part of the scan, close to the group of seven large wind turbines of the Test Centre. For high wind speed, neutral conditions, homogeneity of the wind field is not observed, either for the terrain influence when we are closer to the ground, or, because of the presence of large scale persistence organized structures. The characteristics of these structures in kinematics and two point correlation in terms is analyzed in the following.

#### 4.3. Vertical velocity component at large scales

For mean wind speeds around 15 m/s, the advection of these organized structures across the measurement domain takes place over a period of time of the order of ten minutes. To evaluate their persistence and characteristics, an averaging time window of this length is used to create Figure 4, which represent groups of 13 successive scans during phase 2. Along with the streamwise wind field component, a field of the horizontal velocity divergence,  $\frac{\partial U_1}{\partial x_1} + \frac{\partial U_2}{\partial x_2}$ , is used to evaluate the importance of fluctuations of vertical velocity component,  $U_3$ , relative to the horizontal  $U_1$  and  $U_2$  components. The horizontal wind divergence field is smoothed using a two-dimensional isotropic Gaussian filter, with a spread of a half of the spanwise integral length scale,  $L_{u_1, x_2}$ , in order to smear out the contribution of small eddies and enhance the features of larger scale fluctuations in the energy-containing range. Elongated high and low wind speed streaks can be observed. Low speed streaks correlate strongly with positive values of the smoothed divergence of the horizontal components, which is evidence of upward ejection of parcels of lower streamwise momentum. Such behavior has been observed in results from Large-Eddy simulations [5], laboratory experiments [7], and in atmospheric flow measured by an array of sonic anemometers [1].

From a ‘snapshot’ of the wind field (one scan requiring 45 s) at  $z = 50$  m, such as the one in Figure 5, it is possible to see clearly the randomly distributed and smaller scale ejections/low speed streaks that are smeared out when we average over a 10-minute period (as in Fig. 4). Even though the advection speed at 50 m height is not much lower and the strength of the horizontal divergence is similar to the ones observed at 200 m, these streaks tend to meander and have lateral displacements that cancel out when time-averaged. Figure 6 shows a snapshot at 200 m, where streaks are longer and better defined, features that persist when averaged over 10 minutes, enhancing the inhomogeneity of the wind field. Even though we still observe meandering, the lateral displacements are smaller relative to the streak size.

At 200 m the observed coherent structures maintain a three dimensional nature. Streaks with positive horizontal divergence, caused by vertical ejections of lower momentum flow, can be the signature of streamwise rolls that extend for several kilometers. The picture is clearer when we check the smoothed vertical component of the vorticity shown in Figure 7. When we overlap the wind field with contours of positive divergence we see that the streaks are bounded by counter-rotating vortex lines, consistent with the hairpin-packet structures described by [7] and [17]. Streamwise large scale rolls might show opposite sign vorticity contours at each side of the streak, but what we see is more localized and small scale vorticity that could be the signature of several hairpins’ legs, advected downstream by the main flow as a packet. The lateral separation of opposite-sign vortex pairs reaches some hundreds of meters, making low-speed streaks much narrower than high-speed streaks—which is not the case observed at 50 m.

<sup>1</sup> In effect, above the roughness sublayer

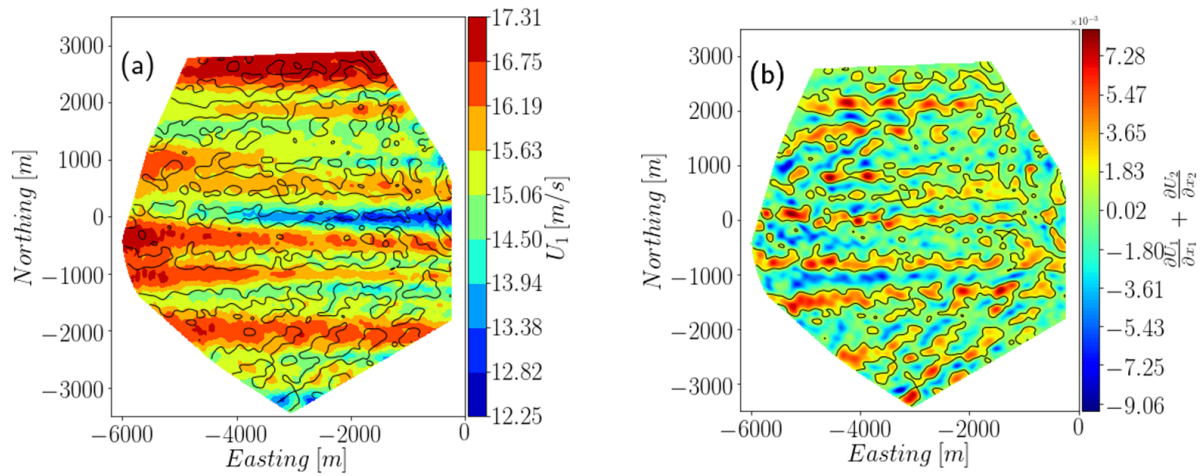


**Figure 4.** (a) 10-minute average of  $U_1$  at  $z = 200$  m above ground level. Contours of positive values of divergence are imposed to highlight their correlation with low momentum streaks (as well as negative divergence correlates with higher speed streaks) (b) Divergence of horizontal wind components,  $\frac{\partial U_1}{\partial x_1} + \frac{\partial U_2}{\partial x_2}$ , showing elongated shapes of positive and negative divergence that start to tear apart as they approach the large wind turbines in the east of the scanning area.

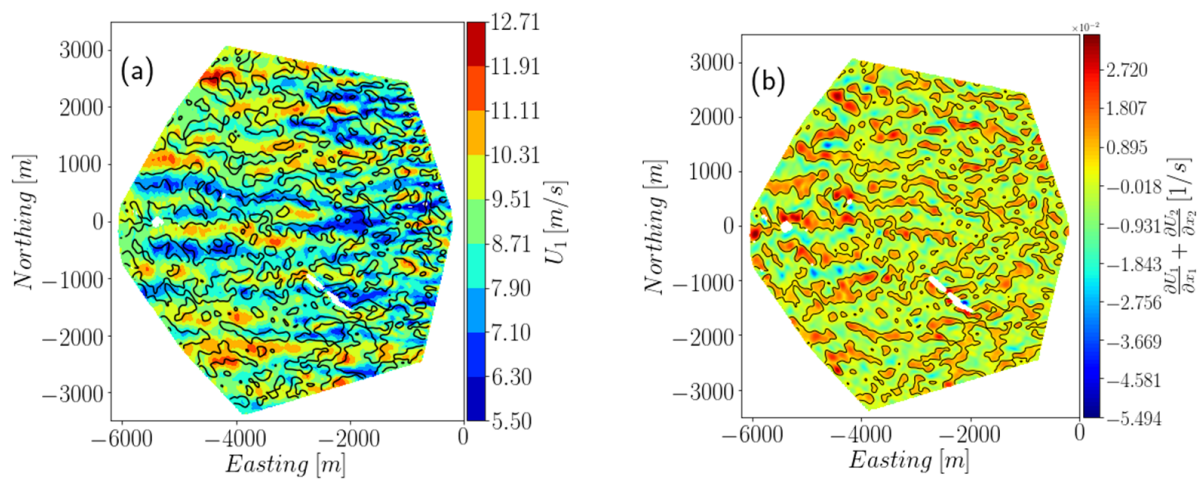


**Figure 5.** Snapshot (45-second scan) of: (a)  $U_1$  field, and (b) horizontal divergence at  $z = 50$  m; contours in (a) correspond to positive divergence in (b). Streaks show smaller length scale closer to the ground and more random locations with lateral displacements that cancel them out when averaged.

#### 4.4. Two-point correlations and integral length scales

Two-point statistics of  $U_1$  fluctuations, give insights into the spatial characteristics of coherent structures. Figure 8 shows the average of instantaneous  $\rho_{uu}$  within a period of 30 minutes (same

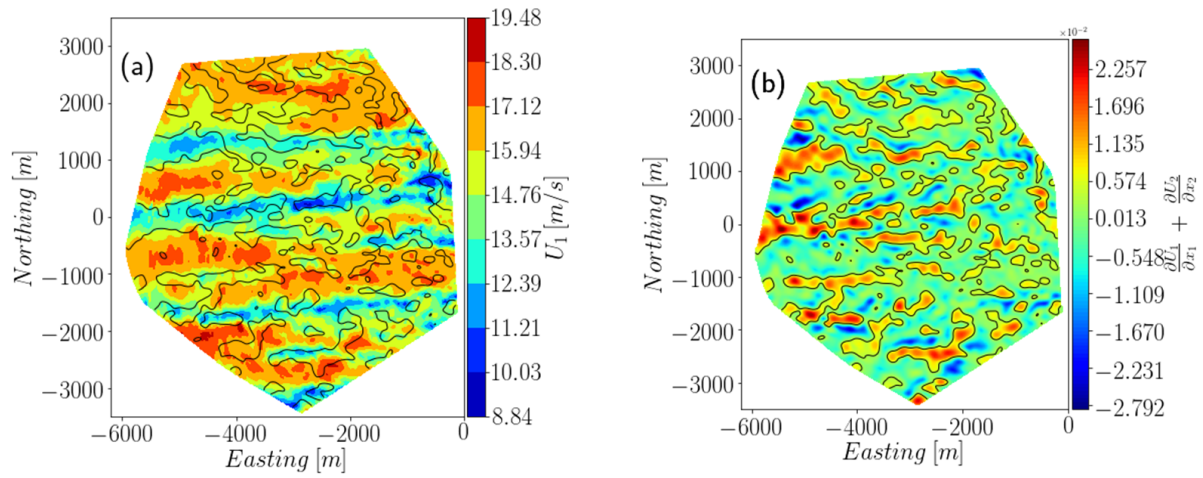


**Figure 6.** Snapshot (45-second scan) of: (a)  $U_1$  field, and (b) horizontal divergence at  $z = 200$  m; for westerly wind. Longer, low-momentum streaks are accompanied by larger ejection areas of positive divergence, shown in (b).

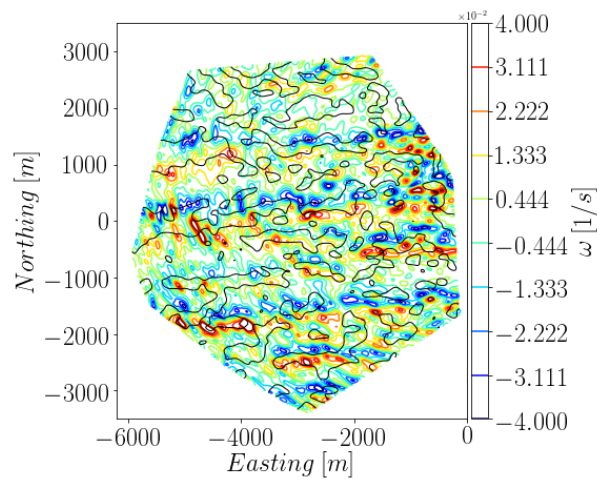


**Figure 7.** Vorticity (color) and positive divergence contours for wind field scan shown in Fig. 6. Ejection zones are bounded by counter-rotating vortices, forming stripes of positive and negative vorticity across the whole domain.

period as in Figure 3) for neutral and high wind speed conditions. Here the lags move along the displacement axis  $(\tau, 0)$  and  $(0, \eta)$  for phase 1 and 2 of the experiment. As can be seen,  $\rho_{uu}(\tau, 0)$  shows long correlation lengths, in contrast with the short correlation in  $\rho_{uu}(0, \eta)$ , evidence of narrow structures extended in the streamwise direction with positive and negative streamwise speed fluctuations. Since the wind fields are mostly inhomogeneous, the fluctuations around

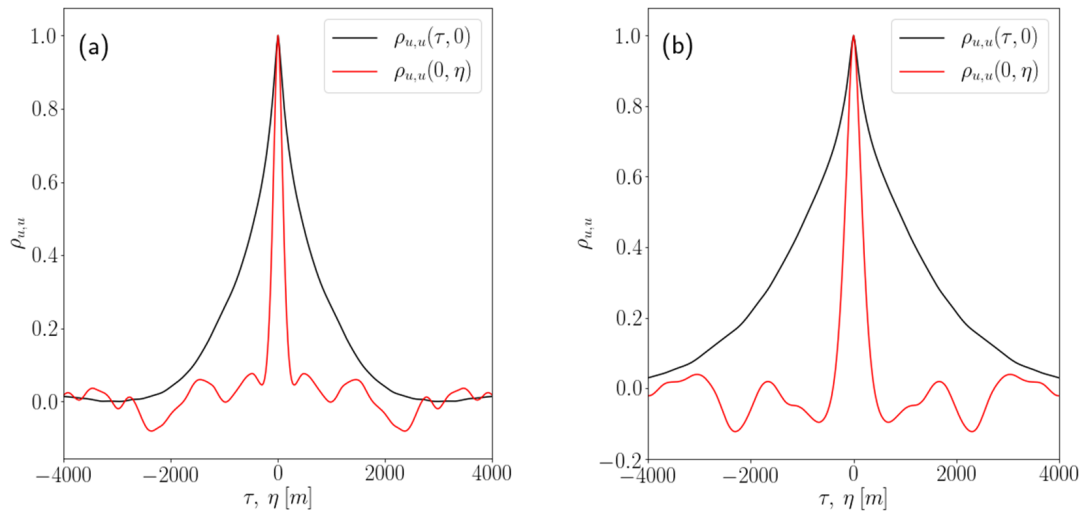


**Figure 8.** Correlation function for stream and spanwise lags,  $\tau$  and  $\eta$ , for the 30 minutes of scanning time in Figure 3 at (a) 50 m and (b) 200 m height. Long correlation length in  $(\tau, 0)$  relative to  $(0, \eta)$  indicate very long and narrow streaks of low momentum, with characteristic separation given by successive peaks in  $\rho_{uu}(0, \eta)$ . This characteristic is more evident at 200 m, with longer and more separated structures.

a predefined mean wind speed, obtained by averaging the whole domain, can lead to peaks of increasing correlation with negative values of  $\rho_{uu}(0, \eta)$  which still will give information about the mean spacing of this elongated structures. In the case shown in the Figure 8 this spacing is around 500m for phase 1 and 1500m for phase 2.

Figure 9 shows pairs of  $L_{u_1, x_1}$  and  $L_{u_1, x_2}$ , for all cases under neutral stability conditions during phase 1 and 2 of the experiment. Even though it takes between 10 and 13 scans for a coherent structures to cross the measuring domain, which make successive wind fields not totally independent, a major part of the cases show values of  $L_{u_1, x_1}$  and  $L_{u_1, x_2}$  corresponding to elongated structures, with  $L_{u_1, x_1}$  going in average up to a 700m at 50 m height and to more than a kilometer at 200 m above the ground level. The integral length scales of the 30 minute average in Figure 8 are highlighted to show their relative position to other neutrally stratified cases. Both wind fields, i.e. referring to respectively 50 m and 200 m, represent cases with large values of  $|L|$ , and well above the limit of stable or unstable stratification. It is possible to see the anisotropy of the larger structures portrayed by integral length scales in both phases. At 50 m height the mean values of  $L_{u_1, x_1}$  and  $L_{u_1, x_2}$  show more proximity to the dashed one-to-one line than at 200 m, where  $L_{u_1, x_2}$  seems to be limited to a range going from 100m to 300m, with large spread in the spanwise length scale, with a mean around 900m. Length scales during phase 1 still show the signature of the long streaks previously seen. A tail with large values of  $L_{u_1, x_2}$  approaching the one-to-one line is observed here and, after inspecting the corresponding values of  $L$ , they show mostly negative values, often seen at night.

## 5. Conclusion and future work

The kinematic and statistical characteristics of large scale coherent structures in atmospheric flow has been explored, using observations made with two wind lidars. The capabilities of this measuring technique are rapidly developing, making it more and more relevant for wind field characterization across different scales. The data collected allowed us to visualize the extent of large-scale organized motions, whose sizes can reach kilometers, making them an

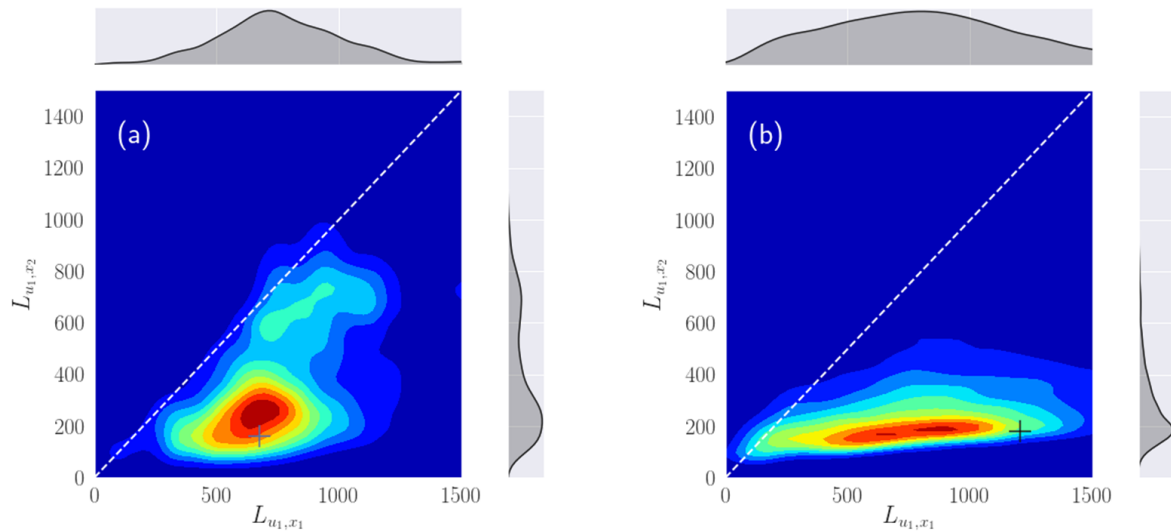


**Figure 9.** Integral length scales for neutral stable cases, (a) phase 1 (50 m a.g.l.) of the Balconies experiment and (b) phase 2 (200 m a.g.l.). The dashed white line marks where  $L_{u_1, x_1} = L_{u_1, x_2}$ , i.e. no directional preference for energy containing scales. Crosses indicate  $(L_{u_1, x_1}, L_{u_1, x_2})$  for cases in Figures 8. Marginal pdf and color scale show frequency.

important factor determining the homogeneity of the atmospheric flow over modern wind farms. Moreover, the influence of these structures on the wind field features increases and changes, as we look at heights above the surface layer that are relevant for modern wind energy production. Nevertheless, the similarities between the results shown here and the ones obtained by numerical and laboratory experiments needs to be extended to different stability and wind conditions. We expect that during unstable or stable flow stratification situations, large scale organized motion will show, if they exist at all, substantial differences from what was presented in this work. Additionally, their interaction with smaller scale turbulent fluctuations, as well as momentum fluxes within scales that can affect the operation of individual turbines, is yet to be explored.

## References

- [1] Hutchins N and Marusic I 2006 *J. Fluid Mech.* **579** 1
- [2] Hutchins N, Chauhan K, Marusic I, Monty J and Klewicki J 2012 *Boundary-Layer Meteorol* **145** 273
- [3] Young G, Kristovich D, Hjelmfelt M and Foster R 2002 *B. Am. Meteorol. Soc.* **83** 997
- [4] Träumner K, Damian T, Stawiarski C and Wieser A 2015 *Boundary-Layer Meteorol.* **154** 1
- [5] Fang J and Porté-Agel F 2015 *Boundary-Layer Meteorol.* **155** 397
- [6] Hussain A 1983 *The Phys. of Fluids* **26** 2816
- [7] Adrian R 2007 *Phys. of Fluids* **19** 041301
- [8] Larsen G, Madsen H, Thomsen K and Larsen T 2008 *Wind Energy* **15** 377
- [9] Vasiljevic N, Lea G, Courtney M, Cariou J, Mann J and Mikkelsen T 2016 *Remote Sens.* **8** 896
- [10] Peña A and *et al* 2015 *Remote Sensing for Wind Energy* (Denmark: DTU Wind Energy)
- [11] Mann J, Angelou N, Arnqvist J, Callies D, Cantero E, Arroyo R, Courtney M, Cuxart J, Dellwik E, Gottschall J *et al.* 2017 *Philos. T. R. Soc. A* **375** 20160101
- [12] Karagali I, Mann J, Dellwik E and Vasiljević N 2018 *J. Phys.: Conf. Series* **145** 052029
- [13] Alcaayaga L 2020 *Atmos. Meas. Tech. Discuss.* **2020** 1
- [14] Lenschow D and Stankov B 1986 *J. Atmos. Sci.* **43** 1198
- [15] Lenschow D, Mann J and Kristensen L 1994 *J. Atmos. Ocean. Technol.* **11** 661
- [16] Kelly M and Gryning S 2010 *Boundary-Layer Meteorol.* **136** 377
- [17] Tomkins D and Adrian J 2003 *J. Fluid Mech.* **490** 37